

Received July 14, 2021, accepted July 22, 2021, date of publication July 26, 2021, date of current version August 4, 2021.

Digital Object Identifier 10.1109/ACCESS.2021.3100311

Calibration Procedure of Camera With Multifocus Zoom Lens for Three-Dimensional Scanning System

JYUN-CHENG HUANG¹, CHIEN-SHENG LIU², (Member, IEEE), AND CHUNG-YU TSAI¹

¹Department of Mechanical Engineering, Advanced Institute of Manufacturing with High-Tech Innovations, National Chung Cheng University, Chiayi, Minhsiung 62102, Taiwan

²Department of Mechanical Engineering, National Cheng Kung University, Tainan 70101, Taiwan

Corresponding author: Chien-Sheng Liu (csliu@mail.ncku.edu.tw)

This work was supported by the Ministry of Science and Technology of Taiwan, under Grant MOST 105-2221-E-006-265-MY5, Grant MOST 106-2628-E-006-010-MY3, and Grant 108-2218-E-002-071.

ABSTRACT With zoom lenses, both the magnification of the camera and the distance between the lens and the object plane can be changed. Changes to zoom lens magnification is accompanied by changes in the depth of field and the distance between the lens and the object plane, complicating the calibration of zoom cameras—specifically, that of each focus and zoom control, for which separate configurations are required. To overcome this problem, a procedure for the calibration of a multifocus zoom lens in a three-dimensional (3D) scanning system was developed in the present study. Specifically, a pragmatic, five-step calibration procedure was proposed. In the first two steps, the characteristics of the zoom lens were obtained. In the third and fourth steps, the calibration was normalized. Finally, the effectiveness of the process was assessed using a laboratory-developed prototype. High reconstruction accuracy was achieved.

INDEX TERMS Active optical scanner, camera calibration, zoom lens, zoom-dependent calibration, reconstruction accuracy.

I. INTRODUCTION

Optical topography measurement has extensive industrial and cultural applications in fields including mechanical engineering, industrial manufacturing, cultural heritage conservation and restoration, and virtual reality [1]. Structured light profilometry is a highly reliable technique for reconstructing the three-dimensional (3D) characteristics of an object. Camera calibration, through which the intrinsic and extrinsic parameters of the camera are obtained, contributes crucially to the accuracy of 3D reconstruction [2]. The calibration of a prime lens for 3D reconstruction conventionally involves the use of a calibration target (taking into account target position and density of features) and standard procedures. In contrast to prime lenses, zoom lenses allow users to adjust the field of view and allow the camera to adapt to different-sized objects according to the situation. Therefore, zoom lenses are more valuable than prime lenses with regard to applications in 3D computer vision and 3D scanning [3].

The associate editor coordinating the review of this manuscript and approving it for publication was Qiangqiang Yuan.

The estimation of calibration parameters typically requires a calibration target with features of a given density that is positioned strategically within a designated framework. Therefore, 3D reconstruction that is based on both standard and prime lens calibration is highly accurate. Numerous studies on prime lens calibration have been conducted [4]–[18]. Developed on the basis of the standard calibration technique, zoom lens calibration techniques comprise linear and nonlinear strategies [19] for setting various lens parameters. Prime lens calibration based on perspective projection is also suitable for zoom lenses [20]–[22]. Multiple studies [23]–[27] have adopted the strategy developed by Tsai [28] for zoom lens calibration, which requires the use of multiple types of calibration targets under various lens settings [29]—a drawback that explains why it has yet to become a common technique [30].

When the setting of a zoom lens changes, intrinsic parameters, extrinsic parameters, or a combination of both are taken as the variadic parameters [19], [23]–[27], [31]–[35], and the setting of each parameter depends on testing configuration and results. By treating all camera parameters as

variadic parameters, Xian *et al.* [33] observed that adjusting the optical settings of the zoom lens leads to variations in the camera parameters. Most studies on zoom lens calibration methods [23]–[26], [31], [32], [35] have demonstrated that changes in distortion parameters are inevitable, but other researchers [27], [33] have ignored these parameters. Still others [19], [34] have recommended the pre-calibration of lens distortion in all circumstances. In determining the relationship between camera parameters and lens settings, Ahmed and Farag [19] examined various strategies, including polynomial fitting, interpolation, and look-up tables. Through interpolation, each model parameter can be obtained at intermediate lens settings. In this context, only the fitting error of the parameters is considered, and the overall calibration accuracy is completely disregarded. In a study by Zhu *et al.* [36], the error of the center point was closely related to the error of the full field. In many cases, the polynomial method cannot follow complex parametric variations, and determining the optimal function is challenging. This problem can be resolved by using the look-up table method.

When the lens setting is changed, the camera parameter will change accordingly. For most off-the-shelf lenses, the relationship between camera parameters and lens settings is too complicated to be modeled accurately. The numerous generic strategies (e.g., polynomial fitting, interpolation, and look-up table) are often used to approximate the relation. Polynomial fitting and interpolation are inferior to the look-up table method with respect to the accuracy of camera and distortion parameter estimates. But, it is impractical to establish a table of motorized lenses through calibration because the step resolution of the motor is usually very high. Hence, a novel zoom lens calibration procedure involving several zoom and focus settings was developed in the present study. Regarding the focus settings, the adjustable focus range of the zoom lens under a designated zoom setting was divided by the depth of field into multiple focus settings. Finally, conventional calibration strategies were applied to estimate the camera and distortion parameters under these lens settings. The proposed procedure is presented in section 3.

II. SYSTEM ARCHITECTURE

Fig. 1 presents the hardware of the 3D scanning system used: a projector (Optoma ML750) and a camera (Basler Ace2500-14gc) with a motorized zoom lens (Computar H6Z0812M). A close-up filter (Green.L, +4, 52 mm) was used to reduce the focus distance of the zoom lens. They were installed on an optical table in a dark room in which the temperature was maintained at 25 ± 1 °C and the relative humidity was controlled. The magnification and focus position were adjusted by controlling the zoom and focus settings of the lens. Notably, all the experimental components were commercially available and easily accessible. The hardware parameters are listed in Table 1.

Because the hysteresis of the zoom lens and the nonlinear mechanical control mechanism cause errors in the zoom lens settings, we proposed a control system capable of image

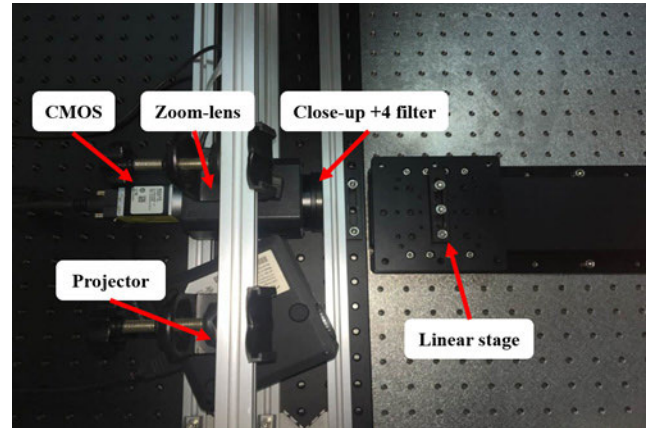


FIGURE 1. Laboratory-built prototype.

TABLE 1. Specifications of laboratory-built prototype.

Item	Serial No.	Specification
Projector	Optoma ML750	Resolution: Wide HD-WXGA (1280×800) Light elements: DLP/LED Standard projection distance:0.55-3.23 m Contrast: 10000:1 Luminosity: 700 ANSI
Zoom lens	Computar H6Z0812M	Angle of view (1/2 type, degree): D: 55.8-9.9, H: 44.6-8.0, V: 33.5-6.1 Focal length: 8-48 mm Object dimension at M.O.D. At 8 mm: 98.4 cm×72.2 cm At 48 mm: 16.8 cm×12.8 cm
Camera	Basler Aca2500-14gc	Sensor size: 2590×1942 Pixel size: 2.2 μm× 2.2 μm Optical size: 1/2.5" Sensor type: Aptina MT9P031 progressive scan CMOS rolling shutter Max. frame rate (at full resolution): 14 fps

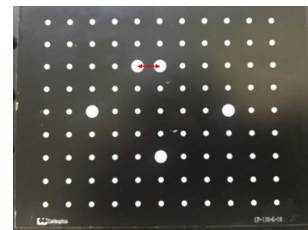


FIGURE 2. Target (CP-130-G-10).

processing. Connected to the serial port of a personal computer, the system microcontroller manipulated the direct current motor through serial communication. To set the zoom lens control system, we placed the target (CP-130-G-10; Table 2) at a fixed position and selected the center of two adjacent large circles as features (Fig. 2). This target is a camera calibration board, and it has two different sizes of circles. The control system can use the image distance between two adjacent large circles as a standard to control the

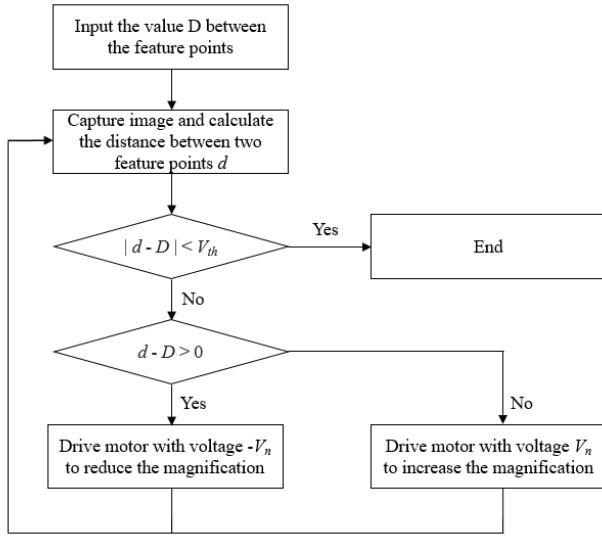


FIGURE 3. Flow chart of proposed zoom control.

TABLE 2. Specifications of laboratory-built prototype.

Item	Serial No.	Specification
Target	CP-130-G-10	Dimension: 130×100 mm Array: 11×9 Circle diameter: 5, 2 mm Center distance : 10 mm

magnification of the zoom lens. The distance between two features was measured in subpixels to determine the zoom setting. Instructions for zoom setting adjustment were sent to the microcontroller through the graphical user interface. As shown in Fig. 3, we first entered a pixel unit value D that was determined by the zoom setting required for the experiment. Second, the camera took a picture and calculated the distance d between the centers of the two features through image processing. Third, if the absolute value of the difference between d and D was less than the threshold, the program ended; if the difference was greater, the d and D values were compared. If $d > D$, the lens setting was adjusted to reduce the magnification; if $d < D$, it was adjusted to increase the magnification. Finally, after the magnification of the zoom lens was controlled, step 2 was repeated until program completion.

To verify the control system, we conducted a simplified experiment. A zoom lens is first calibrated with a target [37] at a fixed (zoom) setting. After accounting for lens distortion, the zoom lens is then to purely zoom with a constant setting of zoom control, each position corresponding to a distance d . The camera photographed the target 10 times under each setting and calculated the distance d between the centers of the two features. The experimental results are presented in Table 3. We can see that the errors are less than 1 pixel.

III. FIXED AND VARIABLE CAMERA MODELS

As shown in Fig. 4 and Eqs. (1)–(3) [38], the fixed camera model (based on the perspective projection theory) describes

TABLE 3. Error experiment using two different zoom control over the 10 times.

Times	Zoom control 1 (pixel)	Zoom control 2 (pixel)
1	-0.5923	-0.1678
2	-0.3175	-0.3921
3	0.0153	0.4543
4	-0.4404	-0.3619
5	-0.1380	-0.3866
6	0.1012	0.5301
7	-0.0055	0.3943
8	-0.2358	-0.3821
9	0.0165	0.2176
10	0.0237	0.2727
Root-mean-square error	0.2201	0.3701

the mathematical relationship among the pixel coordinates, the image plane coordinates, the camera coordinates, and the world coordinates, where $[M_i]$ is the transformation matrix between the pixel coordinates (u_p, v_p) and the image plane coordinates, and $[M_c]$ is that between the image coordinates and the camera coordinates (X_c, Y_c, Z_c) . As the transformation matrix between the camera coordinates and the world coordinates (X_w, Y_w, Z_w) , $[R, t]$ demonstrates the relative orientation of the two coordinate systems in the 3D space, which can be simply represented by the homogeneous coordinate transformation matrix. The matrix represents the features of the camera and the lens, including the pixel size, principal point, skewness, and focal length.

$$\begin{bmatrix} su_p \\ sv_p \\ s \end{bmatrix} = \begin{bmatrix} 1/s_u & \gamma & u_0 \\ 0 & 1/s_v & v_0 \\ 0 & 0 & 1 \end{bmatrix} \begin{bmatrix} u_i \\ v_i \\ 1 \end{bmatrix} = [M_i] \begin{bmatrix} u_i \\ v_i \\ 1 \end{bmatrix} \quad (1)$$

$$\begin{bmatrix} su_i \\ sv_i \\ s \end{bmatrix} = \begin{bmatrix} f & 0 & 0 & 0 \\ 0 & f & 0 & 0 \\ 0 & 0 & 1 & 0 \end{bmatrix} \begin{bmatrix} X_c \\ Y_c \\ Z_c \\ 1 \end{bmatrix} = [M_c] \begin{bmatrix} X_c \\ Y_c \\ Z_c \\ 1 \end{bmatrix} \quad (2)$$

$$\begin{bmatrix} \lambda X_c \\ \lambda Y_c \\ \lambda Z_c \\ \lambda \end{bmatrix} = \begin{bmatrix} r_{11} & r_{12} & r_{13} & T_x \\ r_{21} & r_{22} & r_{23} & T_y \\ r_{31} & r_{32} & r_{33} & T_z \\ 0 & 0 & 0 & 1 \end{bmatrix} \begin{bmatrix} X_w \\ Y_w \\ Z_w \\ 1 \end{bmatrix} = [R, t] \begin{bmatrix} X_w \\ Y_w \\ Z_w \\ 1 \end{bmatrix} \quad (3)$$

where s and λ are the scale factors; s_u and s_v are the horizontal and vertical effective pixel size, respectively; γ is the parameter describing the skewness of the two image axes; (u_0, v_0) are the coordinates of the principal point; f is the focal length; (T_x, T_y, T_z) is the translation along the X , Y , and Z axes, respectively; and r_{ij} are the elements of the 3D rotation matrix, in which i and j both range from 1 to 3 as the row and column indexes, respectively. Combining Eqs. (1)–(3) yields the following equation [30]:

$$sm = A [R, t] M \quad (4)$$

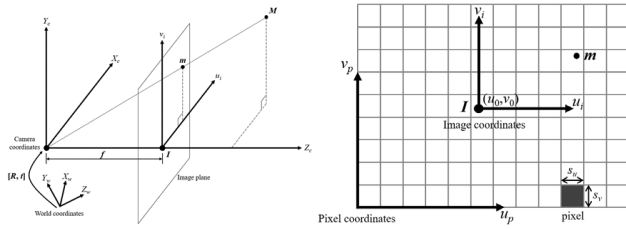


FIGURE 4. Static camera model based on perspective projection theory.

where $[R, t]$ is the extrinsic parameters—that is, the rotation and translation between the camera coordinates and the world coordinates. A , the camera intrinsic parameters matrix, is given by the following matrix equation:

$$A = \begin{bmatrix} \alpha & \gamma & u_0 \\ 0 & \beta & v_0 \\ 0 & 0 & 1 \end{bmatrix}$$

where α and β are the scale factors along the u and v axes of the image plane, respectively, and the focal length function is $f(\alpha, \beta)$. According to the fixed camera model (which is based on perspective projection theory [28]), the following equations are presented:

$$f_\alpha = \alpha^* s_u, \quad f_\beta = \alpha^* s_v,$$

where f_α and f_β are the focal length of the $X_c - Z_c$ and $Y_c - Z_c$ planes, respectively.

Because no lens is perfect, image distortion, especially radial distortion, may introduce errors into the camera model. The lens distortion is main factors hindering us from getting good calibration. Radial distortion is inevitable in the lens manufacturing process, and tangential distortion is produced in the camera assembly process [39]. The effect of the distortion on the pixel coordinates can be undistorted by using the following distortion model:

$$\begin{bmatrix} x_{corrected} \\ y_{corrected} \end{bmatrix} = \begin{bmatrix} x_d \\ y_d \end{bmatrix} + (k_1 r^2 + k_2 r^4) \begin{bmatrix} x_d \\ y_d \end{bmatrix} + \begin{bmatrix} 2p_1 x_d y_d + p_2 (r^2 + 2x_d^2) \\ p_1 (r^2 + 2y_d^2) + 2p_2 x_d y_d \end{bmatrix} \quad (5)$$

where $(x_{corrected}, y_{corrected})$ and (x_d, y_d) are the ideal (i.e., distortion-free) and actual pixel image coordinates, respectively; k_1 and k_2 are the first two radial distortion parameters; and p_1 and p_2 are the tangential distortion parameters. According to Eq. (5), eccentric deformation has both radial and tangential components. The slight tilt of the lens or image sensor can cause distortion of the prism, as well as other radial and tangential distortions.

Imaging models of zoom lenses have been used to calibrate zoom lens cameras. In this study, a camera with automated zoom lenses was calibrated across continual focus and zoom ranges to produce an adjustable perspective-projection camera model. Willson and Shafer [24] used a zoom lens to model the variation in four intrinsic parameters and one extrinsic parameter, the focal length $f(\alpha, \beta)$, the coordinates of the

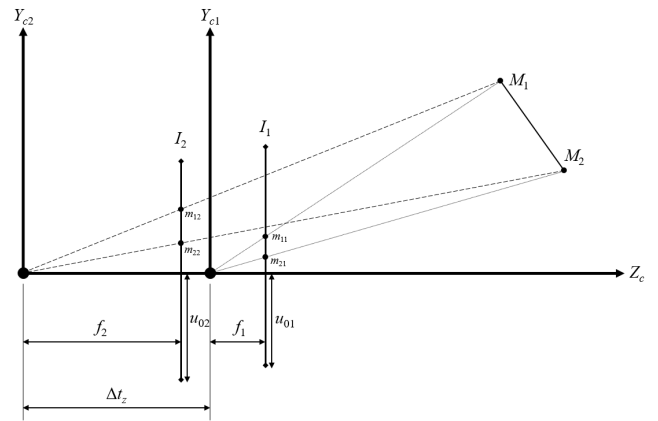


FIGURE 5. Camera model of zoom lens.

principal point (u_0, v_0) , and a translation T_z along the Z axis (Fig. 5). The change in focal length (f) can be determined to be the primary influence on the zoom lens camera model. The secondary influence is the movement of the principal point (u_0, v_0) that is attributable to variations in the optical axis of the zoom lens and the shifting of the origin in the camera's coordinates along the Z axis. Because the zoom lens changes the relative positions of the lens groups, the distortion parameters $[k_1, k_2, p_1, p_2]$ also change.

In conventional calibration strategies [30], the coefficients of intrinsic parameters are obtained before the extrinsic parameters. Regarding the internal parameters, the coefficient of v_0 is first obtained, and the determination of the other coefficients is affected by value of v_0 . The determination of the external parameters is affected by the internal parameter matrix A . As mentioned, the error in the estimation of specific camera parameters is generated when the interactions between the zoom lens parameters are ignored (e.g., polynomial fitting, interpolation.). Therefore, different settings must be applied in the proposed calibration procedure.

IV. PROTOTYPING AND THE PRINCIPLE OF CALIBRATION PROCESS

Manufacturers rarely disclose the functions of zoom lens models. Therefore, the actual relationships between the camera model and the control settings must be determined through several calibration measurements over the working distance of the zoom lens. The present calibration procedure was developed on the basis of multifocus zoom lenses. Because the depth of field and the position of the object plane must be considered under different zoom settings, we divided the calibration procedure into five main steps (A–E; Fig. 6). In steps A and B, the characteristics of the zoom lens were obtained. The mounting of a close-up filter in front of the zoom lens changes its characteristics. Thus, the movable range of the object plane in this magnification setting must be obtained as well as the depth of field of the zoom lens.

As mentioned, a camera with automated zoom lenses was calibrated across continual focus and zoom ranges to produce an adjustable perspective-projection camera model.

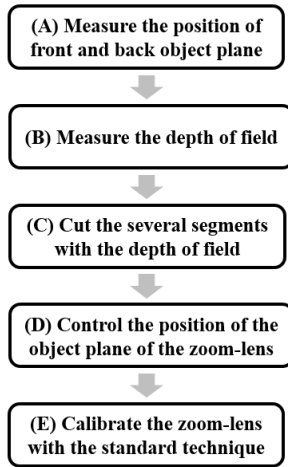


FIGURE 6. Flow chart of proposed calibration procedure of multifocus zoom lens.

The calibration was normalized in steps C and D. To ensure that the zoom lens completely covered the movable range of the object plane, we segmented the range into several focus settings by three-quarters of the depth of field.

A. MEASURING THE FRONT AND BACK OBJECT PLANE POSITIONS

To determine the movable range of the object plane of the zoom lens under this zoom setting, the positions of the front and back object planes must first be measured. Brenner *et al.* [40] proposed a focus measurement method in which the squares of the horizontal first derivative are summed. The function is presented as follows:

$$D(f) = \sum_y \sum_x |f(x + 2, y) - f(x, y)|^2 \quad (6)$$

where $f(x, y)$ denotes the grayscale value corresponding to the pixel position (x, y) . $D(f)$ is the result of the calculation of image sharpness.

As shown in Fig. 7, when the position of the front and back object planes was measured, the setting of the zoom lens was fixed. The camera photographed a Ronchi ruling that was placed as a target on a linear translation stage that was moving continuously and equidistantly. Next, the image sharpness was computed at each position. We used the method proposed by Brenner *et al.* [40] to determine whether the image was in focus and to identify the object plane position of the zoom lens under this setting. As shown in Fig. 8, we positioned the zoom lens to the front and back object planes, in which the maximum values were yielded. In step A, the images of the Ronchi ruling were captured at various positions depending on the distance from the stage. In the end, the positions of the front and back object planes and movable ranges of the object plane were obtained.

B. MEASURING THE DEPTH OF FIELD

As presented in Fig. 9, the image sharpness result obtained at the front object plane position in step A was converted

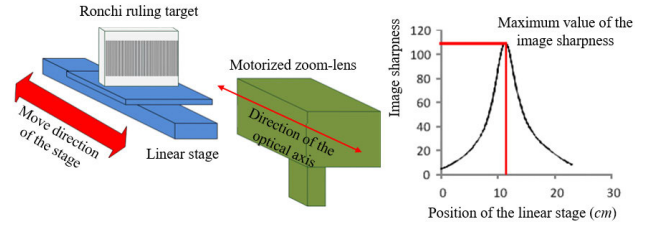


FIGURE 7. Schematic diagram of focus measurement.

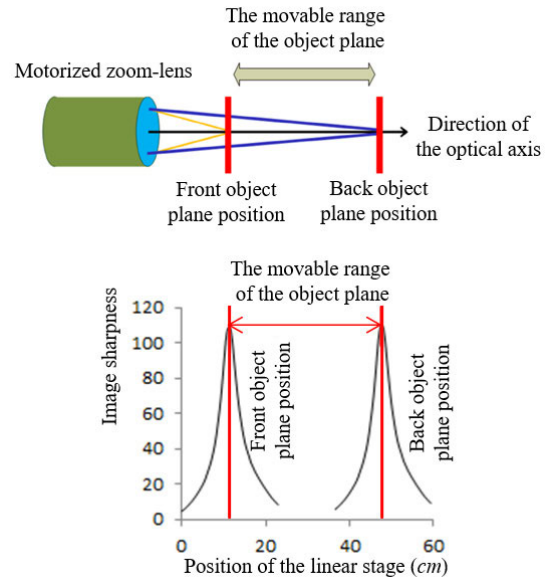


FIGURE 8. Schematic diagram of front and back object plane positions.

and taken as the threshold, and the depth of field was the distance corresponding to the section above the threshold. The threshold was determined by comparing the data with the modulation transfer function (MTF) at the Ronchi ruling. The images were captured at different distances from the stage. The contrast C is calculated by using Eq. (7) as follows:

$$C (\%) = \left[\frac{I_{\max} - I_{\min}}{I_{\max} + I_{\min}} \right] \quad (7)$$

where I_{\max} is the maximum intensity (usually in grayscale pixel values) and I_{\min} is the minimum intensity. We defined the depth of field as a range exceeding 30% of the MTF [44, 45]. In step B, the depth of field was obtained from the result for the front object plane in step A.

C. SEGMENTATION OF THE DEPTH OF FIELD

When the scanned object was not within the depth of field of the zoom lens, the image was blurry. To ensure that the object surface remained within the depth of field, the operator need move the object plane of the zoom lens to the object surface. Segmentation was performed to quantify several focus settings, thereby allowing the efficient performance of the subsequent calibration steps. In steps A and B (Fig. 10), the movable range of the object plane and the depth of field of the zoom lens under this zoom setting were determined.

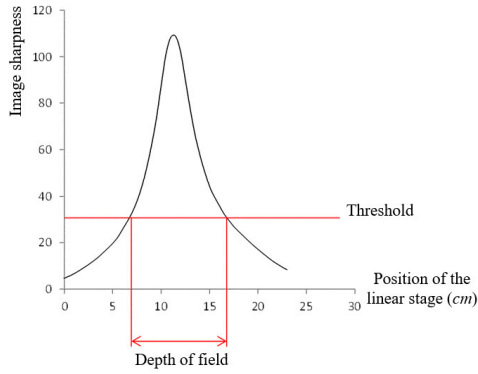


FIGURE 9. Schematic diagram of depth of field.

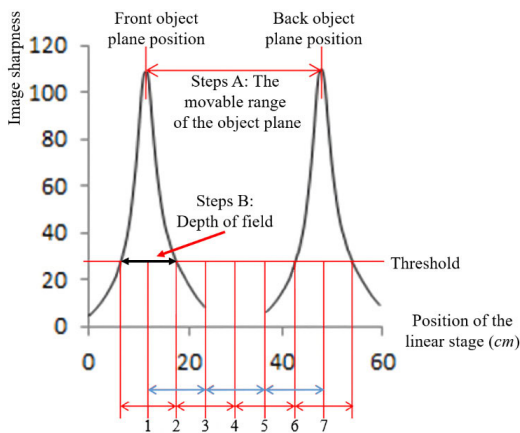


FIGURE 10. Schematic diagram of cut focus settings.

The number of focus settings required under this setting were obtained through a simple calculation. Although the measurement data of the images located at the edge of the depth of field were valid, clear images must be captured. The focus setting was quantified by using three-quarters of the depth of field [43]. In step C, the movable range of the object plane was segmented into several focus settings on the basis of the depth of field.

D. CONTROLLING THE POSITION OF THE ZOOM LENS OBJECT PLANE

To ensure that the object plane of the zoom lens was located at the position we designated in step C, we developed another control system capable of image processing to manipulate the position of the object plane of the zoom lens, which is the function of step D. As presented in Fig. 11 (a), we first set the zoom lens to the front object plane position. Next, a Ronchi ruling was placed as a target on an electric translation stage that moved to the specified position. Each time the camera captured an image, the image sharpness f_1 was calculated through image processing. We applied a voltage to the motorized zoom lens to increase the distance between it and the object plane (ΔL_1), which moved the object plane backward. Subsequently, image sharpness f_2 was computed.

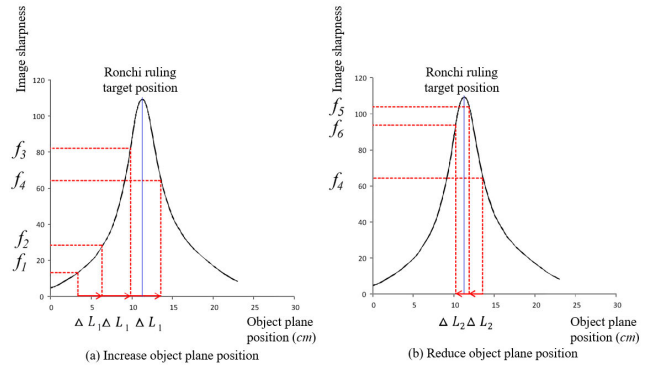


FIGURE 11. Schematic diagram of object plane control: (a) increase object plane position, and (b) reduce object plane position.

When $f_4 < f_3$ after several movements, this indicated that the object plane had passed the specified position (Fig. 11a). Subsequently, we applied a lower reverse voltage to the motorized zoom lens to reduce the distance between it and the object plane; moreover, we moved the object plane by ΔL_2 (Fig. 11b). $\Delta L_1 - \Delta L_2$ approximately equals ΔL_2 . When $f_6 < f_5$ after several movements, this indicated that the object plane had again passed the specified position (Fig. 11b). Because of the low voltage, $\Delta L_2 < \Delta L_1$. Through the repetition of these steps, the position of the object plane of the zoom lens closely approached the specified position.

Fig. 12 presents the control system procedure, which is detailed as follows: In step 1, we captured images to compute the image sharpness f_n . In step 2, we applied a voltage V_j to the motorized zoom lens to increase the distance between it and the object plane. In step 3, images were captured to compute the image sharpness f_{n+1} . In step 4, we determined whether f_{n+1} was greater than 100 (this value is based on the experiments); if it was not, step 2 was repeated until it was. If $f_{n+1} > 100$ from the beginning, we proceeded to the next step. In step 5, we compared the values of f_{n+1} and f_n . If $f_{n+1} > f_n$ and the difference between the two was greater than the threshold, then the object plane had not reached the Ronchi ruling, and that step 2 must be repeated to move the object plane. However, if $f_{n+1} < f_n$, then the object plane had passed the Ronchi ruling, and we proceeded to step 6. In step 6, we applied a reverse voltage V_{j+1} to the motorized zoom lens to reduce the distance between it and the object plane. Because this voltage was smaller than V_j , the extent of object plane movement was lower. In step 7, images were captured after movement and the image sharpness f_{n+2} was calculated. In step 8, we compared the values of f_{n+2} and f_{n+1} . In step 9, if the difference between f_{n+2} and f_{n+1} surpassed the threshold value, then the object plane had not reached the Ronchi ruling, indicating that step 6 should be repeated. However, if $f_{n+2} < f_{n+1}$ at the outset, then the object plane had passed the Ronchi ruling, indicating that the object plane should be moved under continual voltage reduction. In V_j ($j = 0, 1, 2, \dots$), the larger the value of j , the smaller the voltage. In steps 5 and 8, we first determined whether the difference

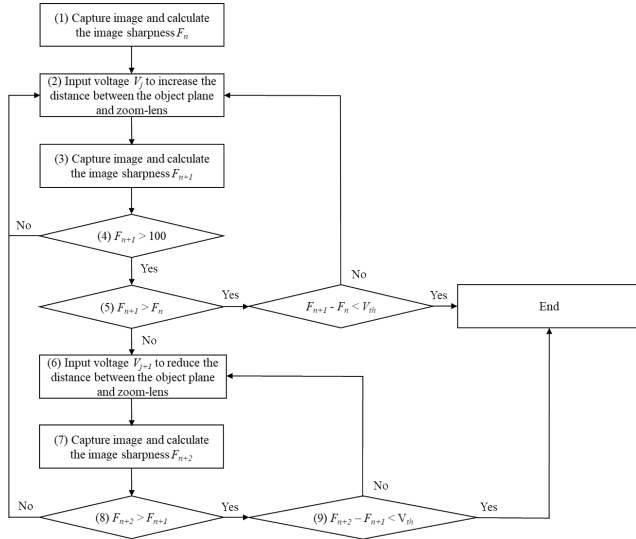


FIGURE 12. Flow chart of proposed focus control.

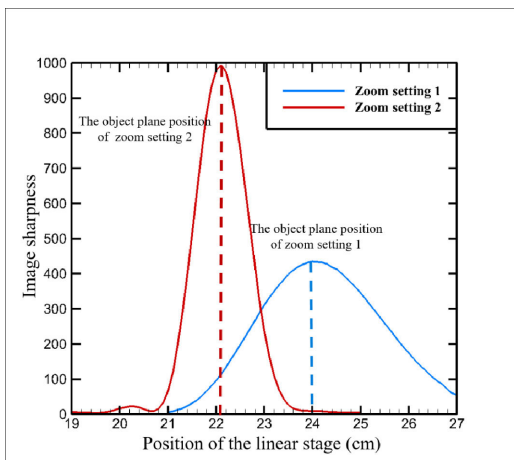


FIGURE 13. Different object plane positions of zoom lens.

between f_{n+1} and f_n and the difference between f_{n+2} and f_{n+1} were less than the threshold; if so, the procedure ended.

E. ZOOM LENS CALIBRATION

In this step, the calibration target was set on the linear translation stage, which was moved to the specified position along with the object plane of the motorized zoom lens. Conventional calibration strategies and a projector codec were used to calibrate the 3D scanning system and determine the calibration parameters for each focus setting. The conventional approach requires the preparation of a calibration target to ensure accurate parametric estimations. Therefore, this strategy yields highly accurate results [44]. The scanning system can be calibrated by using the toolbox in OpenCV 2.4.3, an open source computer vision and machine learning software library [38]. Finally, the calibration parameters for each focus setting can be obtained.

To reconstruct 3D models, the photograph of the object is subjected to image processing [38], which includes the decoding and registration of 3D point clouds. The decoding

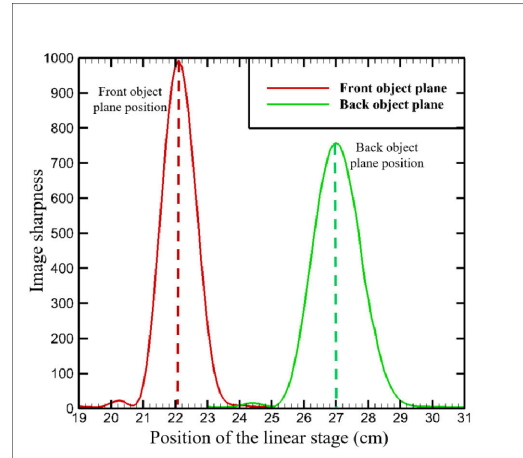


FIGURE 14. Front and back object plane positions of zoom setting 2.

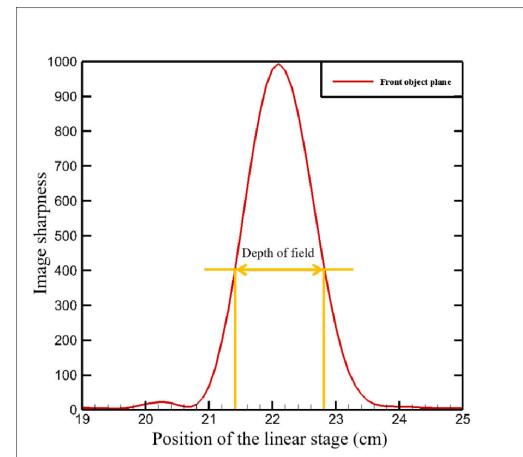


FIGURE 15. Measurement for depth of field.

is performed to correspond the image plane of the projector to the image plane of the camera by using the structured light such that the projector functions as another camera [45]. For the registration, the 3D point clouds of the object are reconstructed. This process involves calculating the optimal depth value through quadratic interpolation. Relevant details can be found in ref. [38].

V. EXPERIMENTAL CHARACTERIZATION

As indicated in our previous study [38], to improve the accuracy of the reconstruction results, scanning can be performed at a magnification that matches the size of the object (zoom setting 1). Subsequently, the complex area of the object can be rescanned at high magnification (zoom setting 2). However, when the magnification of the zoom lens (focal length) changed, the object plane (focus position) and the depth of field of the zoom lens also changed. As shown in Fig. 13, when the zoom setting was changed from 1 to 2, the position of the object plane moved from 24 to 22.1 cm. Furthermore, the depth of field decreased with the increase in focal length [46], causing the image to become blurry. Thus, the zoom lens must refocus on the object surface.

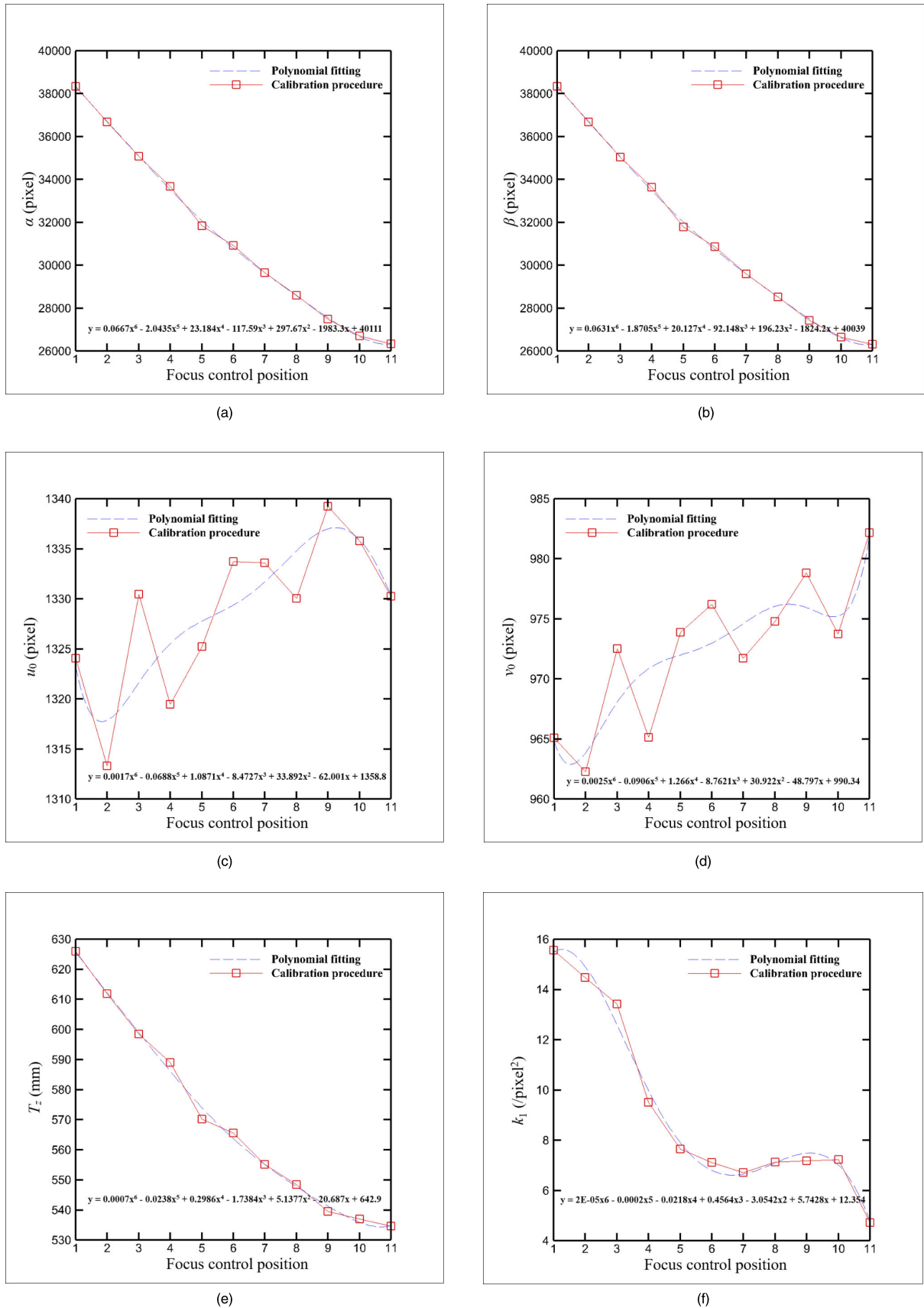


FIGURE 16. Variation of α , β , u_0 , v_0 , T_z , k_1 , k_2 , p_1 , and p_2 on focus control position.

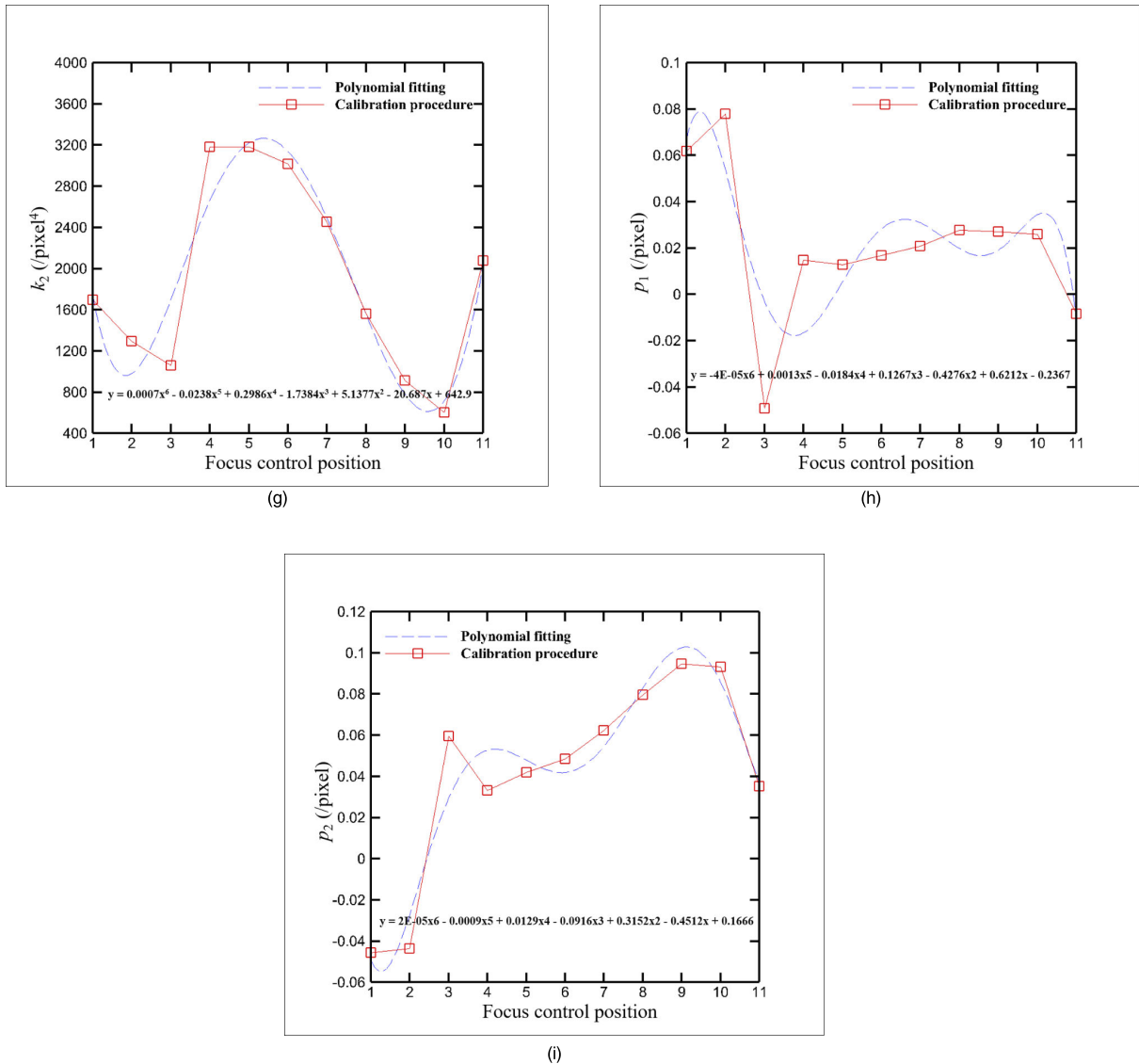


FIGURE 16. (Continued.) Variation of α , β , u_0 , v_0 , T_z , k_1 , k_2 , p_1 , and p_2 on focus control position.

In the experiment, the field of view in zoom setting 1 was double that in zoom setting 2 (Fig. 13), and the distance d between the centers of the two features of zoom settings 1 and 2 were 434.2 and 614 pixels (Fig. 2), respectively. For 3D scanning systems equipped with a zoom lens, multiple focus settings must be implemented after zoom settings are changed. Specifically, we used a laboratory-developed prototype to verify the proposed procedure for multifocus zoom lens calibration. The steps are presented as follows:

In step A, we determined the position of the front and back object planes in zoom setting 2 (22.1 and 27.0 cm from the lens, respectively; Fig. 14). In step B, the measurement results were used to compute the depth of field, which at between 21.4 and 22.8 cm from the lens was 1.4 cm (Fig. 15). In step C, to completely account for the moving range of the object plane in zoom setting 2 (22.1–27.0 cm), and by using three-quarters of the depth of field to quantify the focus setting, we set 11 focus control positions (F_1 – F_{11}) at 22.1,

23.1, 23.6, 24.1, 24.6, 25.1, 25.6, 26.1, 26.6, and 27.0 cm, respectively. In steps D and E, we used the object plane control procedure described in step D in section 4 to ensure that the object plane reached each focus control position (F_1 – F_{11}). Calibration was performed once at each focus control position, yielding 11 calibration files in zoom setting 2. The camera parameters of each focus control position are shown in Fig. 16. The diagrams of α and β (Fig. 16a and 16b, respectively) show smooth variations. The principal point (u_0 , v_0) diagrams (Fig. 16c and 16d, respectively) demonstrate substantial fluctuations relative to the focal length that are attributable of the design of the optical lens [33]. Further research is warranted to detect the connections between each parameter that cause inaccurate estimations of the principal point [37, 50]. The T_z diagram (Fig. 16e) indicates a downward trend, with fluctuations at some focus control positions, that is consistent with the T_z diagram constructed by Willson [25]. The changes in the distortion parameters,

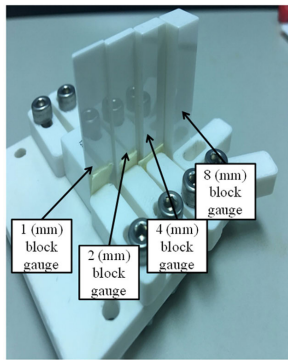


FIGURE 17. Photo of precise block gauges.

which are related to the function of the zoom lens, are shown in Fig. 16f–16i. Specifically, these parameters are equivalent to a deviation of more than 10 pixels from the undistorted image in the edge region of the image.

In many cases, polynomials cannot follow complex variations in certain model parameters. Some researchers used other alternative methods, such as Chebyshev polynomials, and Legendre polynomials. But the issues about the optimal function are still difficult to answer. The look-up table method has been used to solve this problem. The method we propose is similar to the look-up table method. The difference is that we use the depth of field and the range of the object plane to normalize the number of calibrations. And we had taken into account that when the magnification of the zoom lens changed in practical application, the object plane and the depth of field of the zoom lens also changed accordingly. However, the look-up table method did not consider this issue.

We compared the sharpness of the object image at each focus control position, observing a relative maximum value at F6. To verify the performance of the proposed procedure, the reprojection errors of the projection matrix at F6 under the procedure were compared with those under the conventional polynomial fitting procedure (Fig. 16). The parameters for F6, obtained through the polynomial fitting of all the focus control positions, were compared with the parameters at F6. The reprojection errors of the projection matrix under the proposed procedure and the conventional polynomial fitting procedure were 0.16 and 4.11 pixels, respectively. And, we used the calibration parameters generated by these two methods to reconstruct the object with the same camera model [30]. We used ceramic block gauges produced by Mitutoyo with thicknesses of 1, 2, 4, and 8 mm to reconstruct the stepped shape of the object. The distance between the block gauges was measured to verify the reconstruction outcomes (Fig. 17). We used 16-mm block gauges as the substrate to reduce substrate-induced errors. As shown in Table 4. The calibration parameters were estimated with notably higher accuracy with the proposed procedure than with the polynomial fitting procedure.

Finally, we conducted 3D reconstruction without placing the testing objects at the object plane position, causing

TABLE 4. Error experiment using two different methods.

	Proposed procedure	Polynomial fitting
2mm Gauge Block	0.0046 mm	0.0339 mm
4mm Gauge Block	0.0064 mm	0.0601 mm
8mm Gauge Block	0.0095 mm	0.1396 mm

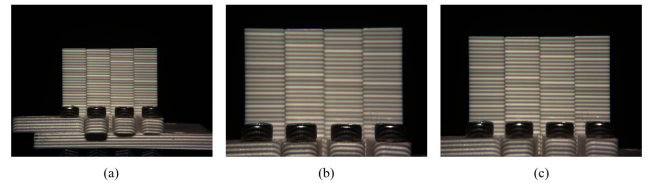


FIGURE 18. (a) Zoom setting 1 (low-magnification and in focus); (b) Zoom setting 2 (high-magnification and out of focus; and (c) Setting 3 (high-magnification and in focus).

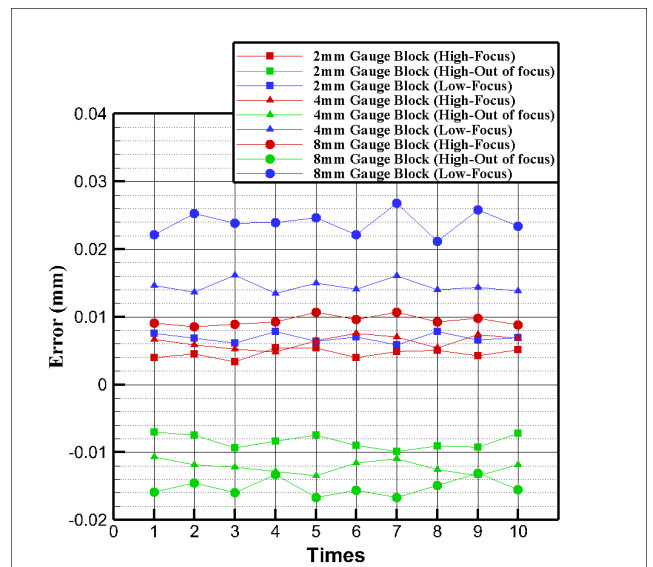


FIGURE 19. Comparison of measurement results for precise block gauges.

defocusing to considerably affect reconstruction accuracy. We performed system calibration for zoom setting 1, zoom setting 2, and setting 3 and photographed the block gauge 24.0 cm from the lens (Fig. 18). Zoom setting 1 was an in-focus, low-magnification setting; zoom setting 2 was an out-of-focus, high-magnification setting (with the zoom setting controlled); and setting 3 was an in-focus, high-magnification setting (with only the focus setting controlled). The camera photographed the block gauge 10 times in each setting, reconstructing the vertical distance between the block gauges (Fig. 19). As shown in Table 5, in zoom setting 1, the average reconstruction errors were approximately proportional to the heights of the block gauges; this is ascribable to the calibration error. Regarding the 4- and 8-mm-thick block gauges, the measurement results were more accurate in zoom setting 2 than in zoom setting 1. In other words, increasing the spatial resolution of the image improved the reconstruction

TABLE 5. The average reconstruction error of block gauges under each experimental setting.

	Setting 3 (F6) (High-Focus)	Zoom setting 2 (High-Out of focus)	Zoom setting 1 (Low-Focus)
2mm Gauge Block	0.0046 mm	-0.0083 mm	0.0071mm
4mm Gauge Block	0.0064 mm	-0.0122 mm	0.0146 mm
8mm Gauge Block	0.0095 mm	-0.0153 mm	0.0241 mm

results. The results for the 2-mm-thick block gauge were worse because its surface was the farthest from the object plane, reducing image sharpness. A sharp image is a prerequisite for satisfactory reconstruction. The results for setting 3 were more accurate than those in zoom setting 2. Overall, the results verify the necessity and accuracy of the proposed calibration procedure. In sum, after the zoom setting changed, the zoom lens required refocusing to yield an enhanced reconstruction image.

VI. CONCLUSION

In this study, a five-step calibration procedure for multifocus zoom lenses was presented. Its accuracy was confirmed through measurements of four gauge blocks performed using a laboratory-developed prototype. The results indicate that changes in the depth of field and position of the object plane should be considered after the magnification of the zoom lens is increased. The proposed method completely accounted for the focus range of the zoom lens at various magnifications, thereby improving the reconstruction accuracy of the 3D scanning system in specific focus settings for a desired depth of field. The proposed procedure can serve as both a theoretical and practical reference for the application and development of zoom lenses in 3D scanning systems. However, before commercial optical scanners apply it in real-world settings, we must achieve the following to enhance reconstruction accuracy. First, we must design a strategy through which several different magnifications can be set automatically such that the first magnification of the zoom lens can be automatically adjusted depending on the sample size. Second, we must develop an algorithm for the automatic determination of the distance between the object surface and the lens such that the scanner can automatically select the appropriate focus settings and calibration parameters.

REFERENCES

- [1] S. Barone, P. Neri, A. Paoli, and A. V. Rationale, "3D acquisition and stereo-camera calibration by active devices: A unique structured light encoding framework," *Opt. Lasers Eng.*, vol. 127, p. 10589, Apr. 2020.
- [2] R. Juarez-Salazar and V. H. Diaz-Ramirez, "Flexible camera-projector calibration using superposed color checkerboards," *Opt. Lasers Eng.*, vol. 120, pp. 59–65, Sep. 2019.
- [3] D. Wan and J. Zhou, "Stereo vision using two PTZ cameras," *Comput. Vis. Image Understand.*, vol. 112, no. 2, pp. 184–194, Nov. 2008.
- [4] A. Zisserman and R. I. Hartley, *Multiple View Geometry in Computer Vision*. Cambridge, U.K.: Cambridge Univ. Press, 2003.
- [5] D. Liebowitz and A. Zisserman, "Metric rectification for perspective images of planes," in *Proc. IEEE Comput. Soc. Conf. Comput. Vis. Pattern Recognit.*, Jun. 1998, pp. 482–488.
- [6] P. Gurdjos, A. Crouzil, and R. Payrissat, "Another way of looking at plane-based calibration: The centre circle constraint," in *Proc. Eur. Conf. Comput. Vis. (ECCV)*, 2002, pp. 252–266.
- [7] F. Qi, Q. Li, Y. Luo, and D. Hu, "Camera calibration with one-dimensional objects moving under gravity," *Pattern Recognit.*, vol. 40, no. 1, pp. 343–345, Jan. 2007.
- [8] F. Qi, Q. Li, Y. Luo, and D. Hu, "Constraints on general motions for camera calibration with one-dimensional objects," *Pattern Recognit.*, vol. 40, no. 6, pp. 1785–1792, Jun. 2007.
- [9] Z. Zhang, "Camera calibration with one-dimensional objects," *IEEE Trans. Pattern Anal. Mach. Intell.*, vol. 26, no. 7, pp. 892–899, Jul. 2004.
- [10] P. Hammarstedt, P. Sturm, and A. Heyden, "Degenerate cases and closed-form solutions for camera calibration with one-dimensional objects," in *Proc. 10th IEEE Int. Conf. Comput. Vis. (ICCV)*, Oct. 2005, pp. 317–324.
- [11] F. C. Wu, Z. Y. Hu, and H. J. Zhu, "Camera calibration with moving one-dimensional objects," *Pattern Recognit.*, vol. 38, no. 5, pp. 755–765, May 2005.
- [12] P. F. Sturm and S. J. Maybank, "On plane-based camera calibration: A general algorithm, singularities, applications," in *Proc. IEEE Comput. Soc. Conf. Comput. Vis. Pattern Recognit.*, vol. 1, Jun. 1999, pp. 432–437.
- [13] X. Meng and Z. Hu, "A new easy camera calibration technique based on circular points," *Pattern Recognit.*, vol. 36, no. 5, pp. 1155–1164, May 2003.
- [14] C. Matsunaga and K. Kanatani, "Calibration of a moving camera using a planar pattern: Optimal computation, reliability evaluation, and stabilization by model selection," in *Proc. Eur. Conf. Comput. Vision (ECCV)*, vol. 1843, Apr. 2003, pp. 595–609.
- [15] L. Huang, Q. Zhang, and A. Asundi, "Flexible camera calibration using not-measured imperfect target," *Appl. Opt.*, vol. 52, no. 25, pp. 6278–6286, 2013.
- [16] F. Yang, Y. Zhao, and X. Wang, "Camera calibration using projective invariants of sphere images," *IEEE Access*, vol. 8, pp. 28324–28336, 2020.
- [17] L. Chen, F. Zhang, and L. Sun, "Research on the calibration of binocular camera based on BP neural network optimized by improved genetic simulated annealing algorithm," *IEEE Access*, vol. 8, pp. 103815–103832, 2020.
- [18] C. Yu, F. Ji, and J. Xue, "Dynamic granularity matrix space model based high robust multi-ellipse center extraction method for camera calibration," *IEEE Access*, vol. 8, pp. 128308–128323, 2020.
- [19] M. Ahmed and A. Farag, "A neural approach to zoom-lens camera calibration from data with outliers," *Image Vis. Comput.*, vol. 20, nos. 9–10, pp. 619–630, Aug. 2002.
- [20] L. Agapito, E. Hayman, and I. Reid, "Self-calibration of rotating and zooming cameras," *Int. J. Comput. Vis.*, vol. 45, no. 2, pp. 107–127, Apr. 2002.
- [21] S. N. Sinha and M. Pollefeys, "Pan-tilt-zoom camera calibration and high-resolution mosaic generation," *Comput. Vis. Image Understand.*, vol. 103, no. 3, pp. 170–186, Sep. 2006.
- [22] E. Hayman and D. W. Murray, "The effects of translational misalignment when self-calibrating rotating and zooming cameras," *IEEE Trans. Pattern Anal. Mach. Intell.*, vol. 25, no. 8, pp. 1015–1020, Aug. 2003.
- [23] M. Sarkis, C. T. Senft, and K. Diepold, "Calibrating an automatic zoom camera with moving least squares," *IEEE Trans. Autom. Sci. Eng.*, vol. 6, no. 3, pp. 492–503, Jul. 2009.
- [24] R. G. Willson and S. A. Shafer, "Perspective projection camera model for zoom lenses," *Proc. SPIE Opt. 3D Meas. Techn. II, Appl. Inspection, Qual. Control, Robot.*, vol. 2252, pp. 149–158, Mar. 1994.
- [25] R. G. Willson, "Modeling and calibration of automated zoom lenses," *Photon. Ind. Appl.*, vol. 2350, pp. 170–186, Oct. 1994.
- [26] W. Zheng, Y. Shishikui, Y. Kanatsugu, Y. Tanaka, and I. Yuyama, "A high-precision camera operation parameter measurement system and its application to image motion inferring," *IEEE Trans. Broadcast.*, vol. 47, no. 1, pp. 46–55, Mar. 2001.
- [27] M. Figl, C. Ede, J. Hummel, F. Wanschitz, R. Ewers, H. Bergmann, and W. Birkfellner, "A fully automated calibration method for an optical see-through head-mounted operating microscope with variable zoom and focus," *IEEE Trans. Med. Imag.*, vol. 24, no. 11, pp. 1492–1499, Nov. 2005.
- [28] R. Y. Tsai, "A versatile camera calibration technique for high-accuracy 3D machine vision metrology using off-the-shelf TV cameras and lenses," *IEEE J. Robot. Autom.*, vol. JRA-3, no. 4, pp. 323–344, Aug. 1987.
- [29] M. Tapper, P. J. McKerrow, and J. Abrantes, "Problems encountered in the implementation of Tsai's algorithm for camera calibration," in *Proc. Australas. Conf. Robot. Automat.*, 2002, pp. 66–70.

- [30] Z. Zhang, "A flexible new technique for camera calibration," *IEEE Trans. Pattern Anal. Mach. Intell.*, vol. 22, no. 11, pp. 1330–1334, Nov. 2000.
- [31] Y.-S. Chen, S.-W. Shih, Y.-P. Hung, and C.-S. Fuh, "Simple and efficient method of calibrating a motorized zoom lens," *Image Vis. Comput.*, vol. 19, no. 14, pp. 1099–1110, Dec. 2001.
- [32] R. Atienza and A. Zelinsky, "A practical zoom camera calibration technique: An application on active vision for human-robot interaction," in *Proc. Austral. Conf. Robot. Automat.*, Nov. 2001, pp. 85–90.
- [33] T. Xian, S.-Y. Park, and M. Subbarao, "New dynamic zoom calibration technique for a stereo-vision-based multiview 3D modeling system," *Proc. SPIE Opt. East Int. Soc. Opt. Photon.*, vol. 5606, pp. 106–116, Dec. 2004.
- [34] J. García, R. Thoranaghatte, G. Marti, G. Zheng, M. Caversaccio, and M. A. G. Ballester, "Calibration of a surgical microscope with automated zoom lenses using an active optical tracker," *Int. J. Med. Robot. Comput. Assist. Surg.*, vol. 4, no. 1, pp. 87–93, Mar. 2008.
- [35] M. Y. Kim, S. M. Ayaz, J. Park, and Y. J. Roh, "Adaptive 3D sensing system based on variable magnification using stereo vision and structured light," *Opt. Lasers Eng.*, vol. 55, pp. 113–127, Apr. 2014.
- [36] C. Zhu, S. Yu, C. Liu, P. Jiang, X. Shao, and X. He, "Error estimation of 3D reconstruction in 3D digital image correlation," *Meas. Sci. Technol.*, vol. 30, no. 2, Jan. 2019, Art. no. 025204.
- [37] Z. Wu and R. J. Radke, "Keeping a pan-tilt-zoom camera calibrated," *IEEE Trans. Pattern Anal. Mach. Intell.*, vol. 35, no. 8, pp. 1994–2007, Aug. 2013.
- [38] J.-C. Huang, C.-S. Liu, P.-J. Chiang, W.-Y. Hsu, J.-L. Liu, B.-H. Huang, and S.-R. Lin, "Design and experimental validation of novel 3D optical scanner with zoom lens unit," *Meas. Sci. Technol.*, vol. 28, no. 10, Sep. 2017, Art. no. 105904.
- [39] G. Bradski and A. Kaehler, "Learning OpenCV: Computer vision with the OpenCV library," *IEEE Robot. Autom. Mag.*, vol. 16, no. 3, p. 100, Sep. 2009.
- [40] J. F. Brenner, B. S. Dew, J. B. Horton, T. King, P. W. Neurath, and W. D. Selles, "An automated microscope for cytologic research: a preliminary evaluation," *J. Histochem. Cytochem.*, vol. 24, no. 1, pp. 100–111, 1976.
- [41] H. Kawano, T. Okamoto, H. Nakajima, S. Takushima, Y. Toyoda, S. Yamanaka, T. Funakura, K. Yamagata, T. Matsuzawa, T. Kunieda, and T. Minobe, "Practical design for compact image scanner with large depth of field by compound eye system," *Opt. Exp.*, vol. 22, no. 15, pp. 18010–18019, Jan. 2014.
- [42] *Edmund Optics*. Accessed: Oct. 13, 2020. [Online]. Available: <https://www.edmundoptics.com.tw/knowledge-center/application-notes/imaging/contrast/>
- [43] *Power Assist Instrument Scientific Corp.* Accessed: Oct. 19, 2020. [Online]. Available: http://www.apisc.com.tw/index_eng.html
- [44] B. Cyganek and J. P. Siebert, *An Introduction to 3D Computer Vision Techniques and Algorithms*. Hoboken, NJ, USA: Wiley, 2009.
- [45] D. Moreno and G. Taubin, "Simple, accurate, and robust projector-camera calibration," in *Proc. 2nd Int. Conf. 3D Imag., Modeling, Process., Vis. Transmiss.*, Oct. 2012, pp. 464–471.
- [46] B. London, J. Upton, J. Stone, K. Kobre, and B. Brill, "Photography," in *Plastics*, 8th ed. Hoboken, NJ, USA: Prentice-Hall, 2005.
- [47] S. Satoh, "Simple low-dimensional features approximating NCC-based image matching," *Pattern Recognit. Lett.*, vol. 32, no. 14, pp. 1902–1911, Oct. 2011.



JYUN-CHENG HUANG is currently pursuing the Ph.D. degree in mechanical engineering with National Chung Cheng University, Chiayi, Taiwan. His research interests include 3D optical scanner and camera calibration.



CHIEN-SHENG LIU (Member, IEEE) received the B.S. and M.S. degrees from the Department of Power Mechanical Engineering, National Tsing Hua University, Hsinchu, Taiwan, in 1996 and 1999, respectively, and the Ph.D. degree from the Department of Mechanical Engineering, National Cheng Kung University, Tainan, Taiwan, in 2010. From 2003 to 2011, he worked as a Mechanical Design Engineer with the Industrial Technology Research Institute (ITRI), Taiwan. From 2011 to 2012, he was an Assistant Professor with the Department of Mechanical Engineering, National Central University, Zhongli, Taiwan. He joined the Mechanical Department, National Chung Cheng University, Chiayi, Taiwan, in 2012. Since 2018, he has been a Professor with the Department of Mechanical Engineering, National Cheng Kung University. His current research interests include applications of force sensors, voice coil motors, precision measurement, laser-based auto-focusing module, and opto-electronics sensing.



CHUNG-YU TSAI received the B.S., M.S., and Ph.D. degrees in mechanical engineering from National Cheng Kung University, Tainan, Taiwan, in 1994, 1996, and 2007, respectively. From 1998 to 2000, he was a Mechanical Engineer with Tainan Unique Product and Design Company, Taiwan. From 2000 to 2004, he was a Senior Equipment Engineer with Taiwan Semiconductor Manufacturing Company, Taiwan. From 2007 to 2008, he was a Postdoctoral Researcher with National Cheng Kung University. From 2008 to 2018, he was a Professor with National Formosa University, Yunlin, Taiwan. He is currently a Professor with National Chung Cheng University, Chiayi, Taiwan. His current research interests include skew-ray tracing, sensitivity analysis, optical design, optical metrology, gear design, cam design, mechanism design, multi-axis CNC code design, and CMM metrology.

• • •